ADVANCED FUNCTIONAL MATERIALS
www.afm-journal.de

Femtosecond-Laser-Enabled Printing of a Magnetically Gated Hydrovoltaic Smart Window for High-Performance Solar Regulation

Chao Chen, Long Zhang, Jianhan Wang, Zhaoxin Lao, Sizhu Wu, Youdi Hu,* Yuxin Li,* Wanqun Chen, Dong Wu, and Yanlei Hu**

Superhydrophobic smart windows (SWs) hold great potential for use in self-cleaning, energy-saving green buildings. SWs resembling nepenthes that respond to external stimuli have gained the interest of researchers; however, it suffer from unreliable service stability and inferior optical switching sensitivity, hindering their practical applications. In this study, a three-dimensional (3D) magnet-gated SW fabricated by seeding dual magnetic robotics (DMRs) on a femtosecond-laser-printed superhydrophobic transparent droplet-energy generator is reported. With the help of a remote untethered magnet, coaxially magnetized DMRs with reverse magnetic poles can be shape-morphed between open and closed states, achieving visibility switching (ΔT_{vis} = 86.3%) and solar modulation (ΔT_{sol} = 75.7%) within 1 s. Owing to its characteristic all-solid-state features, the superhydrophobic 3D DMR-SW maintains its superior self-cleaning performance even after over 10 000 high-impact droplet cycles. Notably, the current multi-layered DMR-SW can function as an indoor thermal regulator in hot summers and also as an electric generator (instantaneous voltage of ≈35 V) during rainfall. This novel 3D magnet-gated DMR-SW with fast responsivity, energy conservation, water repellency, robust longevity, and multifunctionality is envisioned to accelerate the advancement of self-cleaning optics, hydrovoltaic green buildings, and others.

1. Introduction

Buildings consume ≈40% of total energy in developed countries,[1] with 50% of residential housing energy being used to regulate indoor comfort primarily for air conditioning.[2] Considering the global endeavor for carbon neutrality, a sustainable solution should be developed to enhance building efficiency.[3] Smart windows (SWs), which use stimuli-responsive materials that respond to temperature,[4] electricity,[5] pH,[6] light,[7] mechanical stress,[8] and other factors,[9] can dynamically modulate the solar spectrum based on the user's requirement and may alleviate the energy crisis.[10] Among these, electrochromic windows exhibit a high standard of controllability and are more commercially available, particularly VO_2-derived products,[11] which are highly reliable devices with streamlined yields. Without an electric field, VO_2 remains in a monoclinic phase-insulated state at room temperature, enabling the passage of solar light. Upon electric stimulation, the temperature of the VO_2 nanomaterials increases above the phase transition temperature (τ_c) with the assistance of Joule heating, transitioning to a tetragonal phase metallic state that reflects the solar spectrum and emits infrared wavelengths to the cold outer space.[12] Considering that VO_2-based SWs demonstrated good solar regulation and thermal emitting abilities, their poor optical transparency (T_{vis} = 45.6%) and inferior solar modulating ability (ΔT_{sol} = 22%) significantly hinder their practical applications.[13]

To further enhance its optical performance, researchers have explored emerging representative SW based on hydrogel materials, such as poly(N-isopropylacrylamide),[14] hydroxypropylmethyl cellulose,[15] hydroxypropyl cellulose,[16] N-vinylcaprolactam,[17] polyampholyte hydrogel,[18] and their hybrids.[19] The hydrogel SWs offer the advantages of high visibility (T_{vis} = 90.82%) and excellent solar-regulating ability (T_{sol} = 81.52%),[20] making them promising candidate materials for next-generation energy-saving buildings. Under cool climatic conditions, hydrogel SWs exhibit a clear appearance and facilitate the penetration of sunlight into warm houses.

C. Chen, L. Zhang, J. Wang
Department of Materials Physics and New Energy Device, School of Materials Science and Engineering
Hefei University of Technology
Hefei 230009, China
E-mail: chaoc11@ustc.edu.cn

Z. Lao, S. Wu
School of Instrument Science and Opto-Electronics Engineering
Hefei University of Technology
Hefei 230009, China

Y. Hu, Y. Li, D. Wu, Y. Hu
Department of Precision Machinery and Precision Instrumentation
University of Science and Technology of China
Hefei 230026, China
E-mail: youdihu@ustc.edu.cn; lyx2254@mail.ustc.edu.cn; huyl@ustc.edu.cn

W. Chen
Maxwell Technology Co., Ltd.
Suzhou 215028, China

The ORCID identification number(s) for the author(s) of this article can be found under https://doi.org/10.1002/adfm.202518211

DOI: 10.1002/adfm.202518211

In sharp contrast, once the indoor temperature rises above the lower critical solution temperature on a hot summer day, the hydrogel SW automatically exhibits a white appearance and self-cools by reflecting the solar spectrum.[21] The underlying mechanism is attributed to reversible hydrated extension and dehydrated agglomeration of the cross-linked polymer chains.[22] Although hydrogel SWs are energy-efficient and highly transparent, they are water-affinitive and prone to contamination by muddy water.[23] Once the muddy water dries, the residual dust particles that dwell on the window surface generate strong light scattering, substantially decreasing the daylight transmission.[24]

Researchers proposed a new type of waterproof SW to address the surface contamination problem. For example, Aizenberg and co-workers reported the first paradigm of slippery SW by mimicking the architecture of Nepenthes plants.[25] Through the self-impregnation of low-surface-tension oils into a porous polytetrafluoroethylene substrate, the window could slip surface droplets at a tilting angle of <5°. This surface could be dynamically switched between a clear and an opaque state in response to a graded mechanical stimulus, and is considered the first-generation slippery SW. Inspired by this classical strategy, numerous slippery SWs triggered by temperature,[26] electricity,[27] chemical solvents,[28] and mechanical stress[29] have been studied by various researchers. By doping the phase-change material paraffin with polydimethylsiloxane (PDMS), Yao et al. reported a temperature-activated slippery SW with exceptional water-repellent features, which prevented the invasion of muddy droplets.[30] Additionally, in a previous study, we developed a Joule-heated slippery SW made of paraffin and porous PDMS, and an underlying silver nanowire heater, capable of reversibly modulating optical transparency by loading/discharging a low voltage of 5 V.[31] The underlying mechanism states that once the surface temperature exceeds the melting point of paraffin owing to Joule heat, the window transitions to a transparent state. In contrast, once the Joule heat is removed, the liquefied paraffin transitions into a solid phase when the window acquires a highly reflective state to block the incident light. Notably, this light manipulator can repel diverse organic and inorganic droplets. These studies have significantly facilitated the experimental and theoretical understanding of stimuli-responsive SWs capable of self-cleaning.

Although significant efforts have been dedicated to the development of advanced slippery SWs, several limitations are observed: (1) Slippery SWs always suffer from severe viscous dissipation, resulting in unreliable operational stability.[25–31] (2) Slippery SWs are triggered to discolor within several minutes, signifying low optical-switching sensitivity.[26–31] (3) To date, 2D planar slippery SWs have always been restricted to a single function;[25–31] If a window could continuously harvest energy from natural rainfall, it would be conducive for a sustainable target. Zhen and coworkers innovatively integrated a rain-energy-harvesting function into the conventional optical window through patterning super-hydrophilic polydopamine coating on a hydrophobic PTFE/ITO/PET substrate, which provides great inspirations for next-generation smart windows.[32] Consequently, developing a 3D multimode SW with robust durability, superior sensitivity, self-cleaning capacity, and hydrovoltaic function is still highly-desirable.

To address these challenges, we propose an ultrasensitive yet robust 3D SW by seeding dual magnetic robotics (DMRs) on a femtosecond-laser-printed superhydrophobic transparent droplet energy generator (DEG) platform. Owing to magnetic coding, DMRs with reverse magnetic poles can be reversibly switched to open or closed states in response to an untethered magnet, achieving an on-demand steering of the optical transmittance between 86.4% and 0.1% within 1 s. As a magnet-gated optical switch, the DMR-armored 3D SW exhibited a high solar modulation (ΔT_{sol}) capacity of 75.7% and a small water-slipping angle of ≈5°, which was superior to most previous 2D windows. The current 3D DMR-SW could retain its superhydrophobic property even with the violent impact of water droplets over 10 000 cycles, resulting in ultra-robust durability. Moreover, the influence of the magnetic doping ratio and magnetic flux on the dimming dynamics was systematically studied. Finally, post the novel integration of magnetic robotics with DEG, the function of DMR-SW as a circuit controller, thermal regulator, and droplet-electricity-generator was successfully demonstrated. This study opens new avenues for 3D SWs with multifunctionality and multimodes, and bridges the gap between soft robotics and optical manipulators.

2. Results and Discussion

2.1. Facile Fabrication of a Magnet-Gated Hydrovoltaic SW

SWs are desired to achieve high-efficiency solar modulation and sustainable hydrovoltaic energy generation simultaneously. The proposed device architecture comprises two key functional units: The first component is a superhydrophobic transparent DEG, which serves as a stiff supporter. The second component is a light-dimming actuator composed of soft DMRs featuring a reverse magnetic dipole moment. The hydrovoltaic mechanism of DMR-SW is illustrated in **Figure 1**a. The interface between the shape-memory polymer (SMP) and indium tin oxide (ITO) forms capacitor C_1, whereas the droplet impacting the superhydrophobic SMP micropillars induces the formation of an electric double layer at the liquid–solid interface, generating a new capacitor C_2.[33] Parallel capacitors (C_1 and C_2) accumulate abundant surface charges.[34] Once the droplet contacts the Cu electrode, another capacitor C_3 is created at the droplet–Cu interface, actuating the charge to transfer along the loop-locked circuit to generate an instantaneous voltage.[35] This phenomenon resembles the behavior of a field-effect transistor (Figure S1, Supporting Information).

For solar modulation, in the absence of magnetic actuation, the DMRs remain upright on the DEG substrate, enabling the passage of the incident solar light. Upon exposure to a remote untethered magnet, the two soft robots turn to a closed status, effectively blocking incoming solar light (Figure 1c). Based on the above principle, we designed a desirable hydrovoltaic magnet-gated SW for indoor thermal modulation in hot weather and harvesting water-based energy during rainy weather (Figure 1b). This novel conceptual hypothesis depends on the fabrication of a superhydrophobic transparent DEG platform and the coaxial magnetization of two soft robots with reverse magnetic poles (Figure 1d).

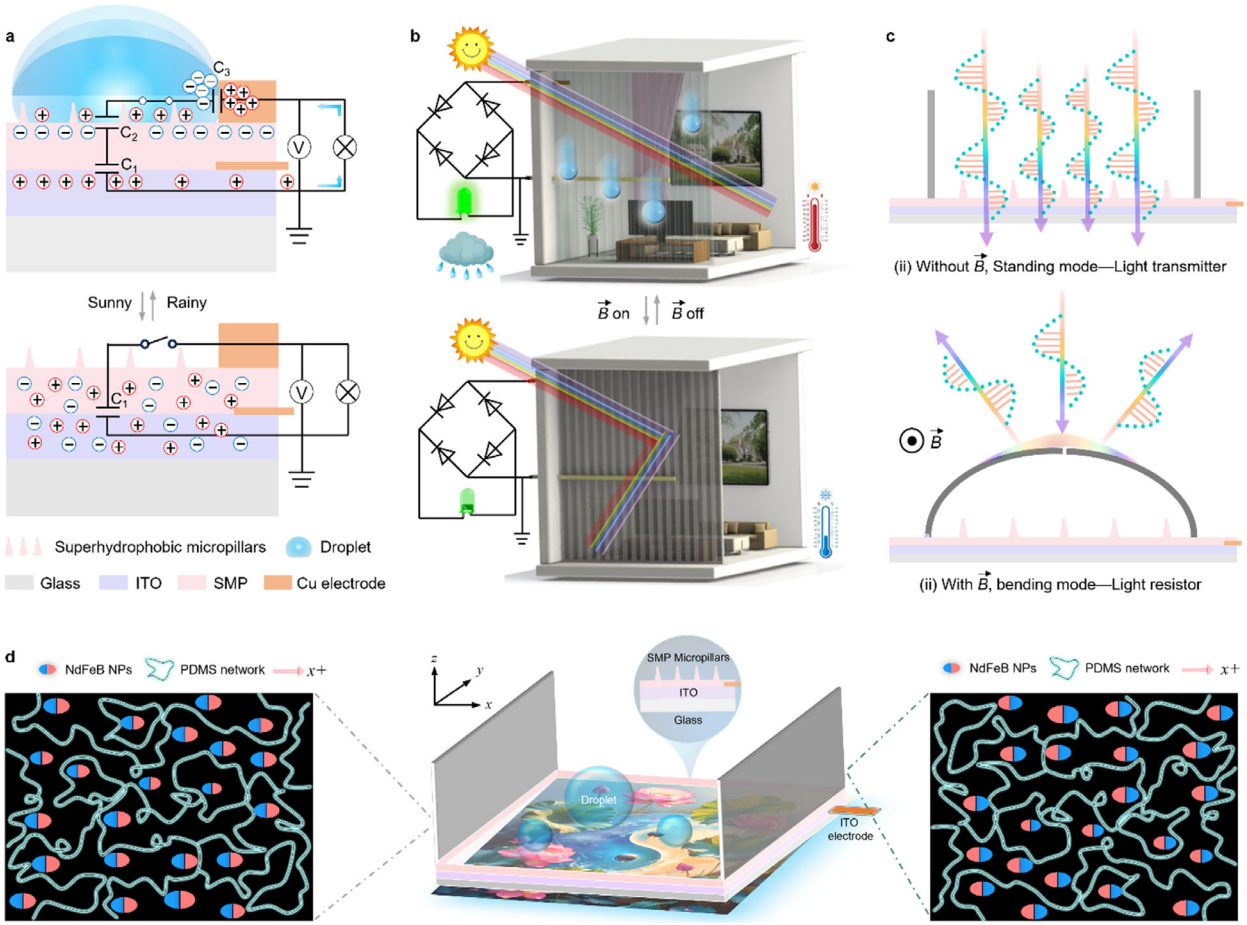

Figure 1. Conceptual hypothesis over a magnetic robotics-actuated hydrovoltaic SW. a) Topological design of a superhydrophobic transparent droplet-energy-generator (DEG) substrate similar to a field-effect transistor structure, including laser-printed superhydrophobic SMP micropillars, ITO glass and Cu electrodes. b) Schematic diagram for displaying a bifunctional SW with solar regulation function in hot weather and DEG function in rainy climate. c) Solar modulating principle for a SW steered by dual magnetic robotics (DMRs) under the aid of a remote untethered magnet. d) Magnetic definition over DMRs with reverse magnetic poles grafted on a superhydrophobic and transparent DEG substrate.

The fabrication of the desired DMR-SW involved eight key steps: (i) A regenerative amplified Ti: Sapphire femtosecond laser system (Legend Elite-1K-HE, Coherent, USA) is used to rapidly ablate a dense array of microholes onto a piece of PTFE film (thickness of ≈100 μm), which serves as a soft transfer template (**Figure** 2ai). The laser power, scanning frequency, scanning cycles, scanning speed, and scanning interval were set as 200 mW, 10 kHz, 10 times, 50 mm s^{-1}, and 300 μm, respectively. Notably, the femtosecond laser with high power density serves as an environmentally benign, high-precision, mask-free, and highly efficient micro/nano-fabrication technology across a wide range of materials, such as polymers, glass, metals, and hard crystals.[36] (ii) Thereafter, the pure SMP precursor is spin-coated (spinning speed: 400 rpm and spinning duration: 30 s) onto the as-prepared template and placed in a vacuum pump for 1 h (room temperature of ≈25 °C) to eliminate air bubbles (Figure 2aii). (iii–iv) Subsequently, indium tin oxide (ITO) glass (resistance R = 14.2 Ω and transmittance at 550 nm T_{550} = 92%) (Figure S2, Supporting Information) was pressed onto the above semi-solidified SMP membrane with a loading pressure of ≈20 N, and then heated and cured at 65 °C for 4 h. Finally, the superhydrophobic transparent DEG substrate was readily harvested by demolding and hydrophobic SiO_2 nanoparticles modification. As shown in Figure 2b,c, scanning electron microscopy (SEM) and laser confocal microscopy reveal that the laser-printed SMP micropillars exhibit a good morphological uniformity (Figure S3, Supporting Information), with height and spacing of ≈110 and 300 μm, respectively. Notably, owing to the cooperation of the SMP micropillars and the hydrophobic SiO_2 coating, the DEG substrate exhibited waterproof properties, including water contact angle (WCA) of ≈153°, and superhydrophobic features, including water sliding angle (WSA) of ≈5° (Figure 2d,e; Figure S4, Supporting Information). Figure 2f further confirms the lyophobic behavior of the transparent DEG in diverse liquids, including inorganic droplets, such as water, and organic species, such as ethylene glycol, coffee, and milk. Owing to its super-hydrophobicity, the transparent DEG can sense the surface falling droplets, generating an instantaneous voltage of ≈30 V in an ultra-short period of 12.5 ms (Figure 2g).

After the achievement of a transparent DEG substrate, DMRs must be integrated for the dimming function. (v–vii) Initially, we infused a uniform neodymium iron boron (NdFeB)/PDMS

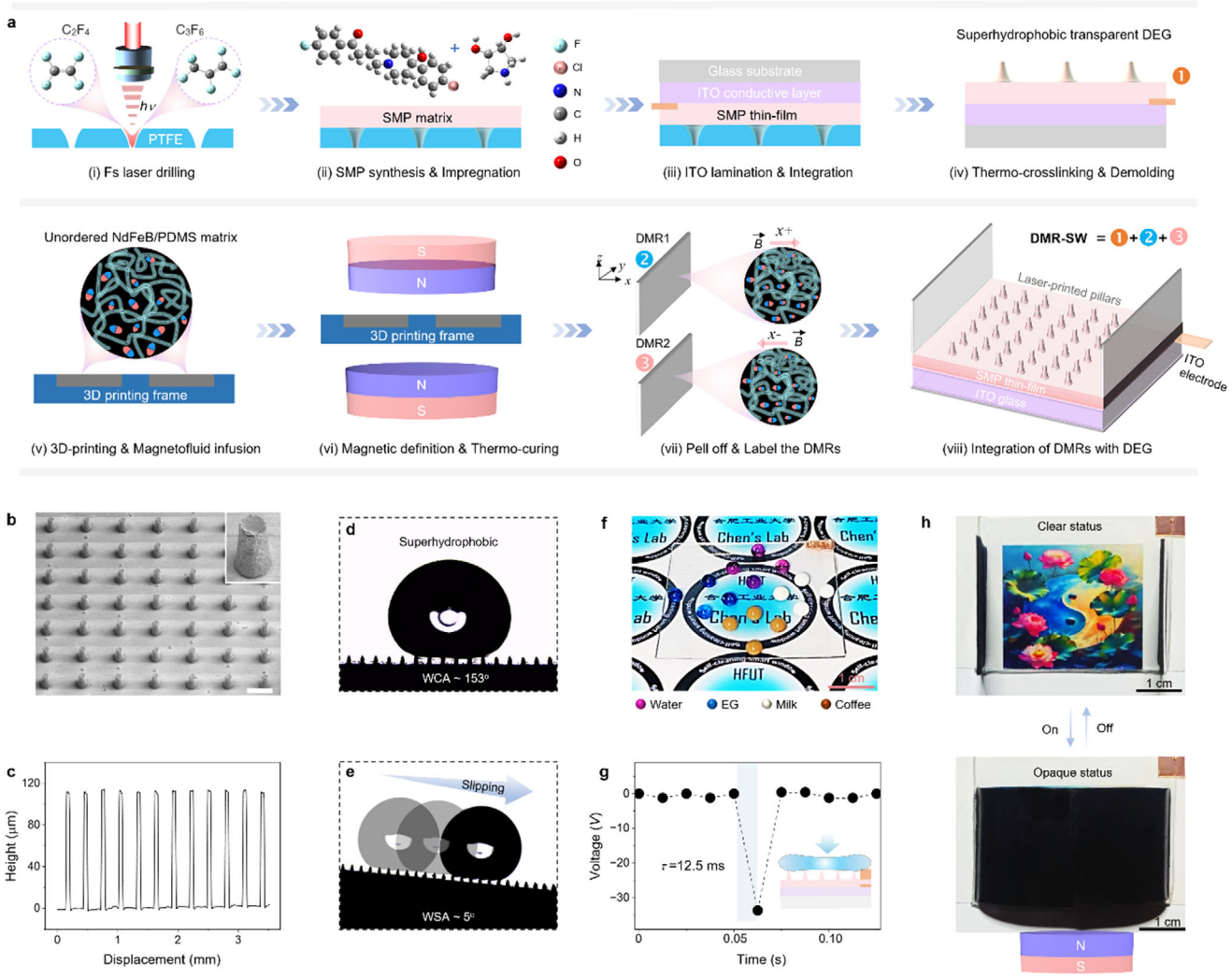

Figure 2. Facile fabrication of a high-performance bifunctional DMR-SW. a) Eight crucial procedures for a hydrovoltaic DMR-SW, including (i) femtosecond-laser-drilling for a microhole template, (ii) impregnation of SMP precursor, (iii) ITO glass lamination, (iv) thermo-crosslinking and soft transfer for a transparent DEG substrate, (v) 3D-printing a magnetofluid (NdFeB/PDMS matrix) reservoir, (vi) Magnetic definition and thermo-curing, (vii) Peeling off and labeling the DMRs, and (viii) Integration of DMRs with transparent DEG platform. b) SEM and c) 3D confocal microscope characterization of the femtosecond-laser-printed SMP micropillar array; The scale bar is 200 μm. The results evidenced that the fabricated microstructures have a good uniformity. Digital clips for displaying the droplet (≈10 μL) wetting performance on the SMP micropillars, including d) water contact angle and e) water sliding angle. f) A digital image for witnessing its robust repellency over diverse liquids (e.g., water, ethylene glycol, milk, coffee). g) Instantaneous electrical power generation of a water drop (≈40 μL) impacting on transparent DEG substrate. h) Reversible optical switching of DMR-SW between a transparent status and an opaque status via steering a remote untethered magnet.

matrix (C = 50 wt.%) into a 3D-printed mold (length × width × depth = 3 × 3 × 0.1 cm). The mold was then sealed and placed between two oppositely polarized magnets for axial magnetization to define the magnetic poles, which was placed at room temperature for 10 h to cure the arrangement of the magnetic chains. Thereafter, the magnetically encoded DMRs were peeled off, and the alignment direction of their magnetic chains was recorded. Finally, DMRs with reverse magnetic poles were arranged onto the as-prepared DEG platform, achieving the terminal establishment of the DMR-SW. By alternately applying and removing the magnetic field, the DMRs could be reversibly switched between the upright and bent states above 1000 cycles, signifying a robust mechanical stability (Movie S1, Supporting information). Owing to their opposite magnetic poles, the DMRs bend inward simultaneously under the same magnetic field, enabling the device to transition between the transparent and opaque states and demonstrating excellent light-adjusting performance, as shown in Figure 2h. By loading/discharging a remote untethered magnet, the optical visibility of the DMR-SW could be reversibly switched between the transparent and opaque states within 1 s (Figure S5, Movie S2, Supporting information). Regarding a large-area window, we can employ the fine-designed electromagnetic coils to control the DMRs separately, which can steer the soft robotics on-demand in a large scope via regulating the applied current, magnetic dimension and scale.[37] As well, by leveraging the optimized arrayed magnets,[38] the current dual soft robotics

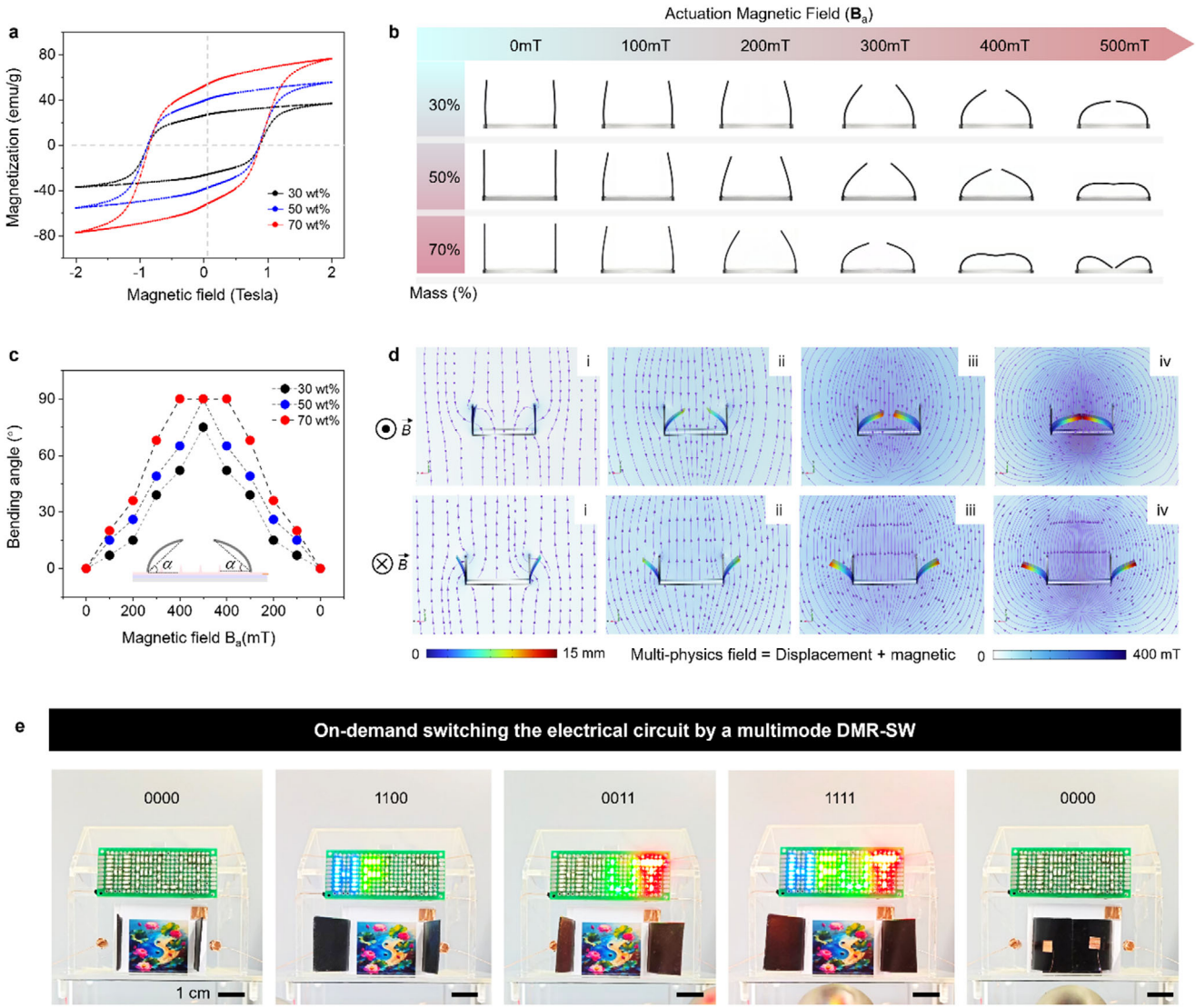

Figure 3. Magnetic actuation of DMR-SW with multimode. a) Hysteresis loops of DMRs with varied NdFeB doping ratio relative to PDMS matrix. b,c) Evolution of DMR bending dynamics as a function of NdFeB doping ratio and B_a. d) Multi-physics field simulation of DMR-SW under the function of a magnetic field. Through varying the location and dimension of a single magnet, the DMR-SW could be readily deformable with multimode. e) Photos for displaying its circuit switching together with optical regulating capability depending on its multimode merit.

as optical dimming units may be precisely manipulated in a large-area extent according to the user's request.

2.2. Magnetically Steering Dynamics Over Reconfigurable DMRs

The deformation is driven by magnetic force (F_m); however, the DMRs recovery depends on the elastic stress (F_{es}) (Figure S8, Supporting information). Therefore, investigating the influence of C_{NdFeB} and actuation magnetic flux (B_a) on the steering dynamics of DMRs is essential (Figure S6, Supporting information). As shown in **Figure 3a**, as C_{NdFeB} increases from 30% to 50% and then to 70%, the corresponding remnant magnetization (M_r) decreases from 52 to 39 emu g^{-1} and then to 26 emu g^{-1}. However, their coercivity (H_c) remained constant at 870 mT. Notably, the maximum B_a used in the experiment was 500 mT, which was lower than H_c, preventing remagnetization and preserving their stable magnetic actuation.[39] In our experiment, C_{NdFeB} has an optimal value. At high values of C_{NdFeB}, NdFeB mixing evenly with the PDMS matrix is extremely difficult, as pronounced agglomeration disrupts the orderly arrangement of magnetic chains during magnetization. However, a lower C_{NdFeB} results in a smaller F_m, which is unfavorable for DMR deformation. Consequently, effective closure of the DMRs to completely block the incident light requires an optimal binary combination (C_{NdFeB}, B_a), which is experimentally confirmed to be (50 wt.% and 500 mT) and (70 wt.% and 400 mT) (Figure 3b,c). Considering the material costs, we selected the former as the optimal combination. To elucidate the deformation and recovery dynamics, we used a multiphysics field simulation to study the

reconfigurable DMR process in response to a locomotive magnet (Figure 3d). The simulation results are consistent with our experimental observations, indicating that the opening and closure of DMRs are determined by the location and dimensions of the magnet. By modulating these two factors, DMRs can be actuated with multiple modes (Movie S3, Supporting information). Taking advantage of this, we steered the DMRs to control a dual-channel circuit composed of blue (B), yellow (Y), green (G), and red (R) light-emitting diodes (LEDs) (Figure 3e). When B_a approached the left side, the left DMR was bent as $F_m > F_{es}$, connecting the "H" and "F" circuits recorded as (1100). Similarly, DMRs can evolve with multimode coupling and decoupling in the range (1111) to (0000), which is envisioned to be conducive to broadening the scope of electronics (Movie S4, Supporting information).

2.3. Optical Switching Performance of a DMR-Armored SW

The DMR-SW can promote daylighting while maintaining privacy by switching between the transparent and opaque magnets. As a light manipulator, it turns transparent without the interference of the magnetic field, with DMRs similar to an open gate; however, it becomes opaque with the function B_a, rendering DMRs similar to a closed gate. For practical applications, SWs are required to exhibit good solar regulation ($\Delta T_{sol} = 75.7\%$) ability and high optical visibility ($T_{vis} = 86.4\%$). In this study, we used UV–Vis-NIR spectroscopy to investigate the optical performance of DMR-SW. As shown in **Figure 4a**, the optical transmittance of the dual-state DMR-SW lies in the range of 400–2500 nm, demonstrating the device's ability to modulate visible and near-infrared spectra; the former determines the SW visibility, whereas the latter dominates the thermal regulating capability. Without a magnetic field, the transmittance at 550 nm (T_{550}, peak sensitivity of the human eye) was measured to be 86.7%, indicating exceptional optical clarity. In contrast, upon magnetic activation, T_{550} decreased to a negligible value of ≈0.1%. As shown in Figure 4b–d, the reflectance (R) and absorbance (A) of DMR-SW can reversibly switch from $R = 9.4\%$ and $A = 3.8\%$ to $R = 4.1\%$ and $A = 95.7\%$, respectively. Notably, DMR-SW can endure the cyclic bending and erecting operation under the functions of F_m and F_{es}, demonstrating good reliability (Figure 4e). We quantitatively analyzed the visible light ($T_{380–780}$), infrared ($T_{780–2500}$), and full-spectrum ($T_{380–2500}$) transmission performance of the dual-mode SW using the following empirical formulae:[40]

$$T_{vis/IR/sol} = \frac{\int \varphi_{vis/IR/sol}(\lambda)\, T(\lambda)\, d\lambda}{\int \varphi_{vis/IR/sol}(\lambda)\, d\lambda} \quad (1)$$

and

$$\Delta T_{vis/IR/sol} = T_{vis/IR/sol}\,(\text{transparent status}) - T_{vis/IR/sol}\,(\text{opaque status}) \quad (2)$$

where, φ_{vis} represents the human eye's photopic efficiency function, and $\varphi_{IR/solar}$ represents the AM1.5 solar irradiance spectrum. In the transparent state, $T_{380–780}$, $T_{780–2500}$, and $T_{380–2500}$ reached 86.4%, 64.5%, and 75.8%, respectively. In contrast, when switched to the shaded state, these values decreased drastically to 0.11%, 0.15%, and 0.13%, respectively. The values of ΔT_{vis} and ΔT_{sol} were 86.3% and 75.7%, respectively. Compared with previously reported SWs, the current DMR-SW is more suitable for high-performance solar regulation owing to its ultrahigh sensitivity, energy-saving merit, electric power generation, self-cleaning, reconfigurable multimode, and good solar-modulating capability (Figure 4f). Among these, the reconfigurable multimode merit enables programmable optical penetration through the DMR-SW by steering the magnetic field (Figure 4g; Movie S5, Supporting information).

2.4. Underlying Hydrodynamics of a Self-Cleaning Feature Over Diverse Liquids

This self-cleaning functionality can protect SWs from contamination by natural sludge and dirt, ensuring their optical clarity and dimming performance.[41] To systematically assess this property, we evaluated the droplet-repellent performance of the DMR-SW substrate by comprehensively measuring the WCA, WSA, and adhesive force (F_a). As illustrated in **Figure 5a,b**, the substrate exhibits superior repellency against inorganic and organic liquids, including water, ethylene glycol, milk, and coffee. High-resolution charge-coupled device measurements were used to measure their WCAs and WSAs (10 µL), where their corresponding values were approximately measured as (156, 145, 13°, and 139°) and (5, 7, 10, and 12°) (Movie S6, Supporting information), respectively. In comparison with the conventional glass ($F_a = 0.8 \times 10^{-6}$ N) and flat SMP membrane ($F_a = 1.3 \times 10^{-6}$ N), the current DMR-SW exhibits a lower interfacial adhesive force ($F_a = 0.4 \times 10^{-6}$ N), which may be attributed to its ultralow surface-free energy (Figure 5c). High-speed imaging further elucidated the distinct droplet dynamics: The DMR-SW surface facilitated rapid droplet rebound with characteristic pancake-bouncing behavior, whereas flat SMP surfaces exhibited strong droplet adhesion without detachment (Movie S7, Supporting information). Quantitative trajectory analysis demonstrates a reduced wetting ridge length (L) and enhanced rebound height (H) on DMR-SW (Figure 5d), corroborating its superior liquid repellency and waterproofing capability. To assess its practical applicability, we evaluated its self-cleaning performance under simulated environmental contamination using dyed particulate matter (Figure 5e). Water droplets efficiently removed surface-bound contaminants, restoring optical clarity without residual fouling, while maintaining high transparency for background visibility. Notably, the efficient elimination of surface contaminants for an excellent self-cleaning feature may rely on the cooperation of floating and lifting removal theories.[42] Significantly, current DMR-SW is resistive to cyclic mechanical rubbing >1000 cycles, demonstrating a good mechanical durability (Figure S7 and Movie S8, Supporting information).

2.5. Solar Regulation and Electric Power Generation via All-In-One DMR-SW

To further evaluate the room-temperature regulation performance of the DMR-SW as an energy-saving window, we simulated direct sunlight using a solar simulator and monitored temperature changes of a PDMS panda pattern (doped with carbon

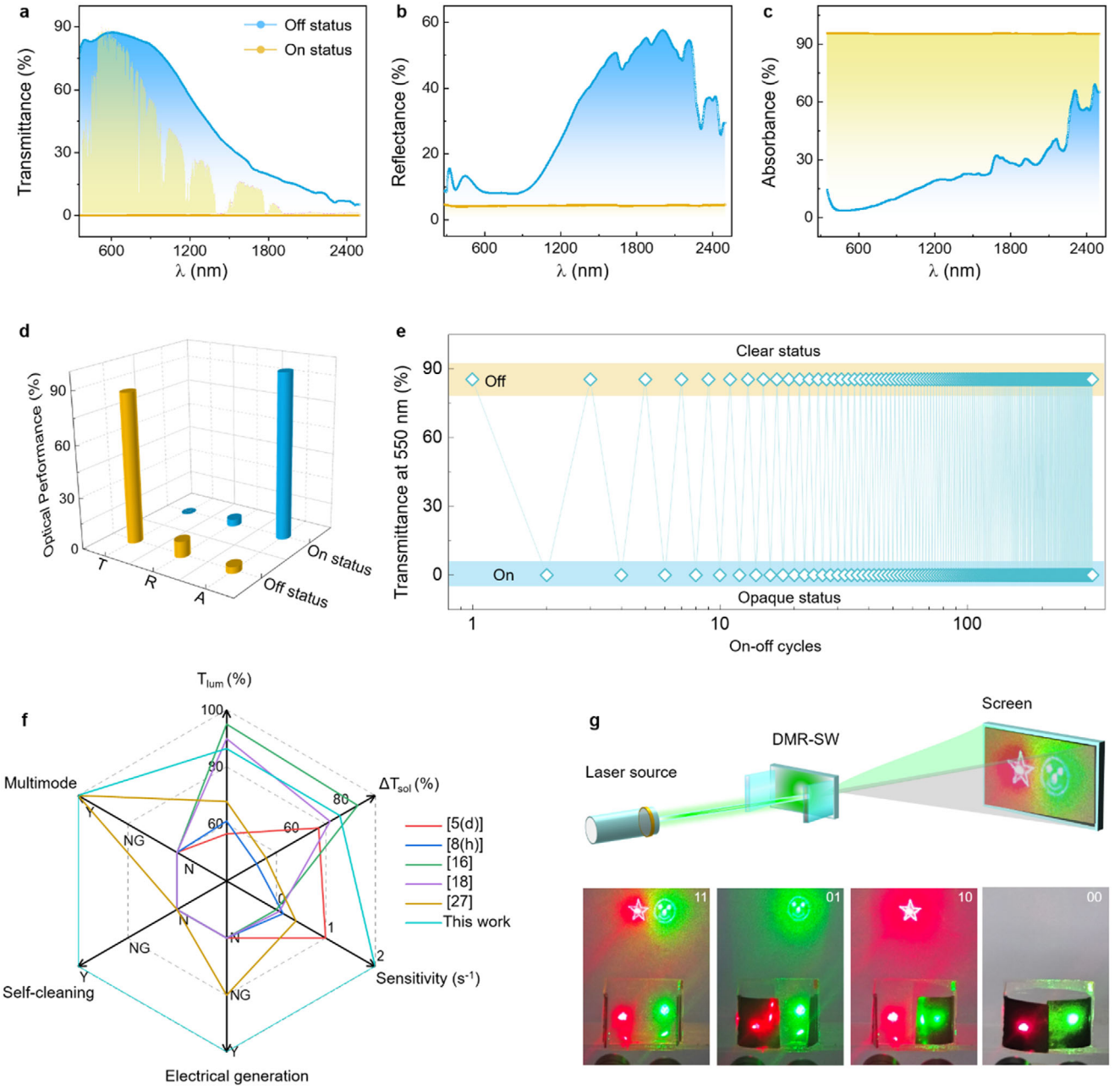

Figure 4. Optical switching performance over DMR-SW. Quantitative analysis of a) optical transmittance, b) optical reflectance, and c) absorbance of dual-state DMR-SW by UV-vis-NIR spectrums. d) Typical optical figures of dual-state DMR-SW at a wavelength of 550 nm. e) Optical switching durability test by cyclic loading/discharging magnetic field. f) Comprehensive performance comparison between current 3D DMR-SW and other conventional 2D SWs. g) Programmable optical transparency on a multimode DMR-SW by fine-tuning the location of a remote magnet.

powder) at the base of a 5 × 5 × 5 cm acrylic model house via thermal infrared imaging. This analysis yielded surface temperature change curves under four shading conditions: air layer, ordinary glass, transparent state, and shaded state. As shown in **Figure** 6a–c, after irradiation for 14 min, the indoor panda temperature reaches 42.6, 41.3, 37.8, and 26.1 °C. Compared to traditional glass windows, the DMR-SW can flexibly and rapidly switch between the transparent and shaded states via magnetic control, achieving superior room-temperature regulation. To optimize the entire droplet-based power generation system, studying the influence of droplet parameters on the output performance is essential after understanding its power generation mechanism. Therefore, we investigated the effects of two parameters: the initial droplet height and tilt angle of the DMR-SW. The experimental results are shown in Figure 6d–g. At four height parameters (10, 20, 30, and 40 cm), the voltage (V) and current (I) exhibited an upward trend with increasing height, peaking at 30 cm (−32 V and −2.1 mA, respectively). This improvement was

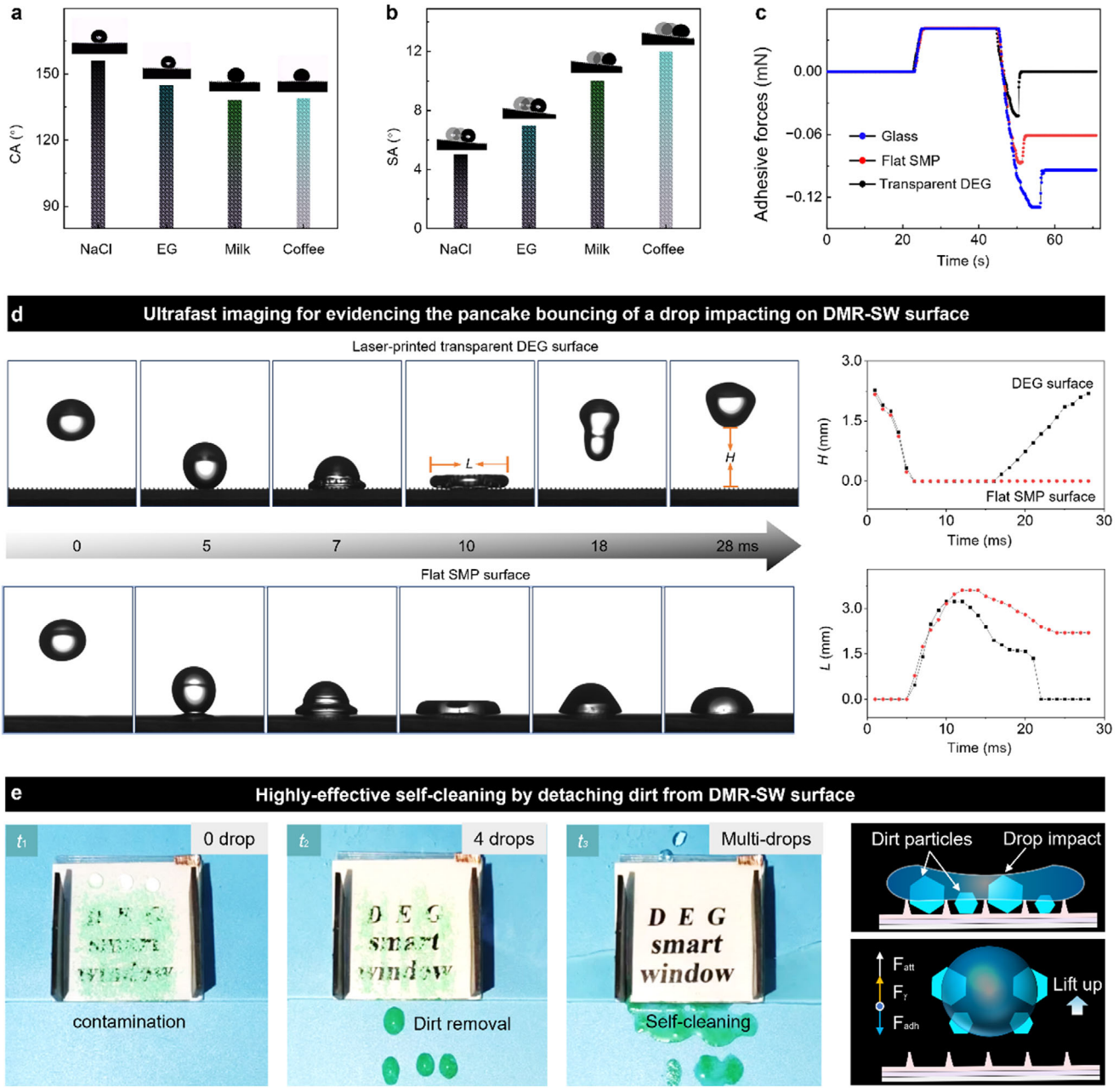

Figure 5. Hydrodynamics over diverse liquids on DMR-SW surface. Characterization of a) contact angles and b) sliding angles over diverse liquids (NaCl, ethylene glycol, milk, coffee, ≈10 µL) on the DMR-SW surface. c) Comparison of the adhesive force for the water droplet (≈10 µL) relative to various surfaces (glass, flat SMP membrane, laser-printed DEG). The result witnesses that DMR-SW has a smaller adhesive force toward a surface drop, signifying a lower drop hysteresis. d) Left side: Time-lapse images for a drop (≈10 µL) impacting on the transparent DEG surface (upper) and flat SMP surface (lower); Right side: Droplet jumping height and wetting length on two different surfaces. The result evidenced that DMR-SW is super-repellent to water droplet on account of the presence of pancake bouncing. e) Self-cleaning function display and its dirt-detaching mechanism.

attributed to an increase in falling height, where the spreading area of the droplet increased upon impact, further increasing the friction area and duration.[43] Consequently, more charge accumulated in the capacitor, leading to a greater charge transfer when the droplet contacted the upper electrode, enhancing the output performance.[44] However, when the falling height reached 30 cm, the droplet spread to its limit, and environmental factors caused instability in the output, resulting in a slight decrease.[45] Similarly, at four angle gradients (15, 30, 45, and 60°), V and I increased with the angle, peaking at 45° (−34 V and −2.1 mA, respectively), followed by a slight decrease. This finding suggests that as the angle increases, the droplet tends to stretch downward along the surface, increasing the friction area and improving the output performance. However, beyond 45°, incomplete surface contact during spreading reduced output performance. Therefore, the falling height and the tilting

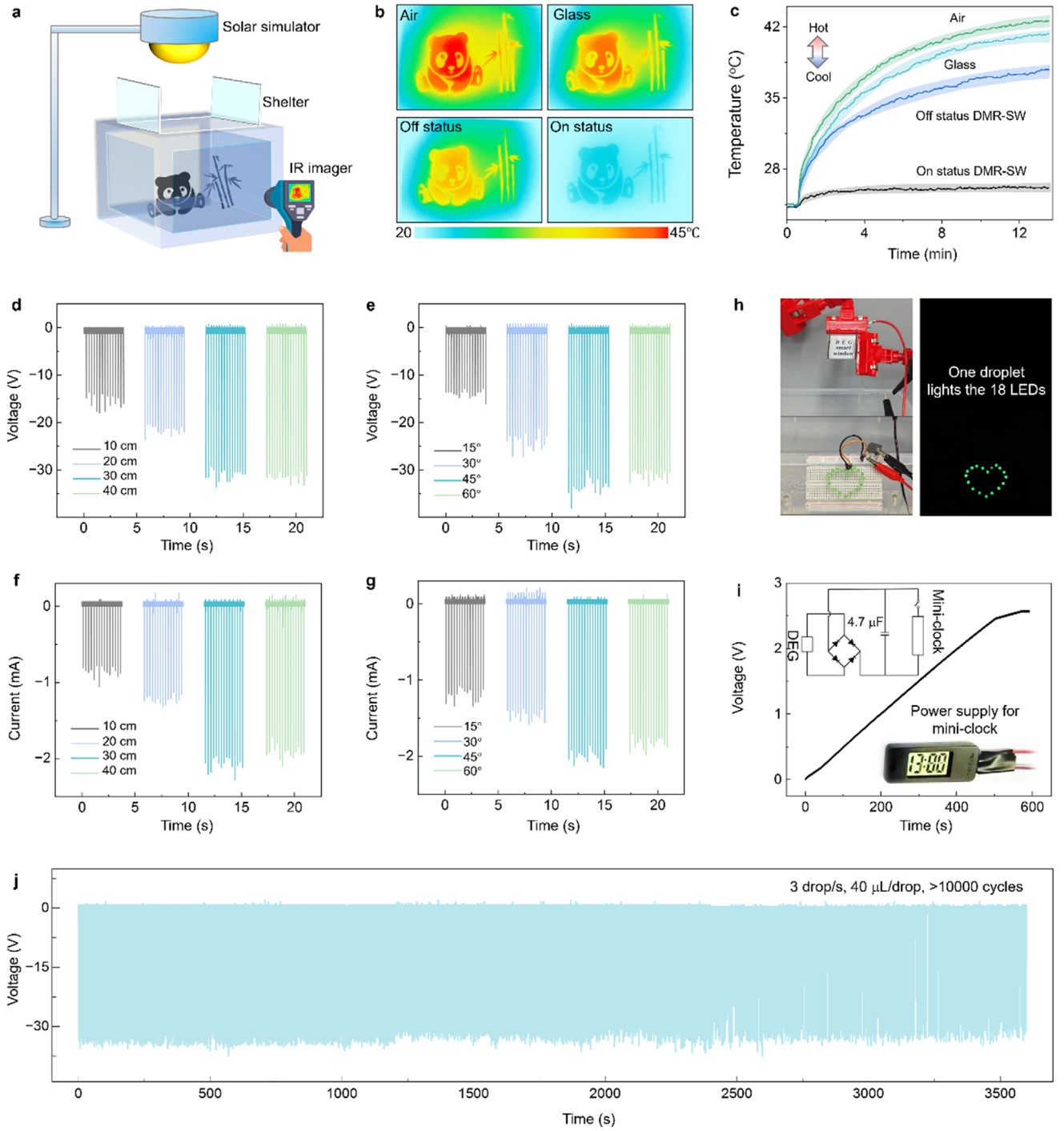

Figure 6. Thermal regulation and hydrovoltaic applications. a) Schematic diagram for displaying a home-built system composed of a solar simulator, open-ended house model, indoor photothermal object, and a hand-hold IR imager. b) IR images and c) temperature-time curves for the roof shelters made by air, glass, off-status transparent (without magnetic field) and on-status opaque (with magnetic field) DMR-SW. d–g) Influence of the droplets impacting distance d and DEG tilting angle α on the electric power generation performance. h) On-site electric power generation by drop (≈40 μL) continuously impacting on a single DMR-SW ($\alpha = 45°$) surface for lighting LEDs. i) Electric power generation and rectification for recharging a mini-clock. j) Longevity test over DMR-SW impacted by continuous and vigorous droplets (≈40 μL) with a frequency of 3 drop/s. The result witnessed DMR-SW has a good durability.

angle must be optimized to achieve superior output performance. Notably, this single DMR-SW can light 18 LEDs based on the hydrovoltaic effect (Figure 6h; Movie S9, Supporting information). Using a home-built rectification system, the instantaneous voltage can be successfully converted to direct current, which can serve as a power source for mini-clock operations (Figure 6i). Moreover, DMR-SW maintains a stable peak output even with >10 000 droplets impacting, demonstrating its ultra-robust durability (Figure 6j). Once current SMP material is substituted by PTFE or FEP with excellent electronegativity as well as charge retention capability, the hydrovoltaic performance is envisioned to be further enhanced.

3. Conclusion

We developed a new magnet-gated SW by integrating dual soft magnetic robotics onto a femtosecond laser-printed superhydrophobic transparent DEG substrate. Owing to the reverse magnetic dipole moment, the DMRs can reversibly switch the optical transmittance between the transparent and opaque states within 1 s, signifying unparalleled dimming sensitivity. Notably, the current DMR-SW also features an admirable T_{vis} of ≈86.4% and a ΔT_{sol} of ≈75.7%, which are superior to most previous products. We quantitatively studied the effect of the NdFeB doping ratio and actuation magnetic field (B_a) on the deformation performance of soft DMRs. Multiphysics field simulations enabled us to further elucidate the multimode deformation dynamics. Moreover, owing to its superhydrophobic properties, DMR-SW can repel diverse liquids to maintain an excellent self-cleaning function. Finally, high-performance solar modulation for indoor comfort regulation and a DEG-aided power supply for mini-clock operation were achieved using an optimized DMR-SW. This study provides valuable insights to researchers for advancing in smart optics, laser micro/nanofabrication, energy conversion, self-cleaning surfaces, and greenhouses, while paving the way for future development in soft-robotics-assisted intelligent windows.

4. Experimental Section

Materials: High-purity NdFeB magnetic particles (purity of ≈99.99% and average size of 5 µm) were purchased from Shanghai Mingjue Trading Co., Ltd. The SMP (shape-memory polymer) material is synthesized by doping the curing agent of polyether-amine-230 into the bisphenol-type epoxy resin precursor with the mass ratio of 1:3, which was purchased from Kunshan Julimei Electronic Materials Co., Ltd. PDMS prepolymer and crosslinker for magnetic blade templating were obtained from Huishan District Chang'an Yifeisi E-commerce Firm. ITO glass substrates were sourced from the Luoyang Luolong District Xuyu New Retail Center. Ethylene glycol was supplied by Sinopharm Chemical Reagent Co., Ltd. Superhydrophobic function was achieved by a hydrophobic spray (SF-04172, Glaco Mirror Coat Zero, Japan), which was purchased from e-commerce platform.

Laser-Writing PTFE Template: The point-by-point circular-scanning (circular diameter ≈20 µm) routine over PTFE templates was ablated by using a regenerative amplified Ti: Sapphire femtosecond laser system (Legend Elite-1K-HE, Coherent, USA). Typically, the scanning power, scanning speed, repeated scanning cycles and scanning area were fixed as 200 mW, 50 mm s^{-1}, 10 times and 4 × 4 cm, where the intervals were set as 0.3 mm. The obtained template was a micro-groove-arrayed topography for a subsequent soft transfer process.

Fabrication of Superhydrophobic Transparent DEG: Based on above PTFE template with micro-hole array, the epoxy resin precursor and curing agent (3:1 mass ratio) were manually blended for 5 min and cast to fully infuse into the microholes under vacuum oven (25 °C, 1 h). Thereafter, a piece of ITO glass (4 × 4 × 0.03 cm) equipped with a Cu electrode (Cu adhesive tape, width × thickness = 2 cm × 100 µm) was laminated onto above semi-product, which could be cured at 65 °C for 4 h. Accordingly, the SMP micropillars were successfully bonding with ITO substrate. Finally, the commercially-obtained hydrophobic coating (SF-04172, Glaco Mirror Coat Zero, Japan) was sprayed on above substrate, and then conducted the spin-coating (1000 rpm, 30 s) and hot assembly (80 °C, 5 min) operation. A fresh superhydrophobic transparent DEG could be prepared.

3D Printing Magnetically-Defined DMRs: A 3 × 3 × 0.1 cm groove template was fabricated using a Bambu Lab P1S 3D printer. The PDMS prepolymer and crosslinker were mixed at a 5:1 mass ratio and stirred for 5 min at room temperature. The mixture was then blended with NdFeB particles at mass ratios of 3:7, 1:1, and 7:3, injected into the template, and degassed for 30 min to eliminate the microbubbles. Curing was performed for 10 h between two opposing cylindrical magnets (at room temperature) before demolding. Finally, we could harvest two pieces of magnetically defined DMRs, which were integrated on the laser-printed superhydrophobic transparent DEG via PDMS media.

Characterization: Field-emission SEM (JEM-2100F, Japan) was used to analyze the microcolumn arrays, and laser confocal microscopy (OLS5100, Olympus) was used to characterize the surfaces of the magnetic smart window (DMR-SW). The adhesion forces were measured using an electronic balance (PX224ZH, Ohaus, USA), and the contact/sliding angles (10 µL droplets) were determined at 10% RH/25 °C using a goniometer (CA100C, Innuo). UV–vis-NIR spectroscopy (3700DUV, Shimadzu, Japan) with an integrating sphere was used to measure transmission and reflection, whereas the absorptivity is obtained from Kirchhoff's Law ($A + R + T = 1$). Droplet dynamics (10 µL) were obtained at 6400 fps using a Photron-SA3 high-speed camera with a Mitutoyo 2× objective. A medical infusion pump was used to generate deionized water droplets at controlled flow-rate intervals. The output voltage was recorded using an oscilloscope (RIGOL DS1104 PLUS, PVP3150 passive probe), and the current was measured using a low-noise preamplifier (SR570, Stanford Research) connected to an electrometer (Keithley 6514). Thermal management analysis was conducted using a solar simulator (CME-Sol 8150, China) and IR thermography (Fotric 348X, China).

Supporting Information

Supporting Information is available from the Wiley Online Library or from the author.

Acknowledgements

This study was supported by the National Key Research and Development Program of China (2024YFB4610700) and Fundamental Research Funds for the Central Universities (Grant No. JZ2025HGTG0269), the Natural Science Foundation of Anhui Province (Grant No. JZ2024AKZR0561), and the National Natural Science Foundation of China (Grant Nos. 52005475, 52305319).

Conflict of Interest

The authors declare no conflict of interest.

Data Availability Statement

The data that support the findings of this study are available from the corresponding author upon reasonable request.

Keywords

droplet-energy-generator, femtosecond laser, magnet-gated transparency, self-cleaning surface, thermal regulation

Received: July 15, 2025
Revised: August 23, 2025
Published online: September 8, 2025

[1] D. M. Kammen, D. A. Sunter, *Science* **2016**, *352*, 922.
[2] M. Isaac, D. P. van Vuuren, *Energy Policy* **2009**, *37*, 507.
[3] L. Pérez-Lombard, J. Ortiz, C. Pout, *Energy Build.* **2008**, *40*, 394.
[4] a) D. Li, C. Zhou, Y. Meng, C. Chen, C. Yu, Y. Long, S. Li, *ACS Appl. Mater. Interfaces* **2021**, *13*, 61196; b) C. Lin, J. Hur, C. Y. H. Chao, G. Liu, S. Yao, W. Li, B. Huang, *Sci. Adv.* **2022**, *8*, 7359; c) J. R. Otaegui, D. Ruiz-Molina, J. Hernando, C. Roscini, *Chem. Eng. J.* **2023**, *463*, 142390; d) A. Roy, H. Ullah, M. Alzahrani, A. Ghosh, T. K. Mallick, A. A. Tahir, *ACS Sustainable Chem. Eng.* **2022**, *10*, 6609; e) G. Xu, H. Xia, P. Chen, W. She, H. Zhang, J. Ma, Q. Ruan, W. Zhang, Z. Sun, *Adv. Funct. Mater.* **2021**, *32*, 2109597; f) X. Zhao, W. Yao, J. Sun, J. Yu, J. Ma, T. Liu, Y. Lu, R. Hu, X. Jiang, *Chem. Eng. J.* **2023**, *460*, 141715.
[5] a) Y. Deng, Y. Yang, Y. Xiao, H. L. Xie, R. Lan, L. Zhang, H. Yang, *Adv. Funct. Mater.* **2023**, *33*, 2301319; b) W. Kamal, M. Li, J. D. Lin, E. Parry, Y. Jin, S. J. Elston, A. A. Castrejón-Pita, S. M. Morris, *Adv. Opt. Mater.* **2021**, *10*, 2101748; c) Y. Li, M. Wang, C. Zhang, C. C. Wang, W. Xu, S. Gao, Y. Zhou, C. T. Wang, Z. Wang, *Adv. Opt. Mater* **2022**, *10*, 2102274; d) J. Yan, X. Fan, Y. Liu, K. Qu, Y. Yu, R.-Z. Li, *Appl. Mater. Today* **2023**, *32*, 101840.
[6] a) J. Guo, S. Wu, Y. Wang, J. Huang, H. Xie, S. Zhou, *Mater. Horiz.* **2022**, *9*, 3039; b) J. He, Q. Zhou, Z. Ge, S. Jiang, J. Li, W. Feng, H. Yang, *Adv. Funct. Mater.* **2024**, *34*, 2404341.
[7] a) W. Meng, Y. Gao, X. Hu, L. Tan, L. Li, G. Zhou, H. Yang, J. Wang, L. Jiang, *ACS Appl. Mater. Interfaces* **2022**, *14*, 28301; b) Y. Wang, Y. Zhao, Z. Yan, T. Li, S. Wang, W. Dong, *ACS Appl. Mater. Interfaces* **2023**, *15*, 43038.
[8] a) T. Alqurashi, H. Butt, *Science* **2019**, *5*, 1002; b) Y. Ke, N. Li, Y. Liu, T. Zhu, S. Wang, Y. Li, G. Lin, Q. Zhang, Y. Hu, Z. Dong, J. Yin, Z. Liu, Y. Long, *Adv. Funct. Mater.* **2023**, *33*, 2305998; c) J. Li, X. Lu, Y. Zhang, X. Ke, X. Wen, F. Cheng, C. Wei, Y. Li, K. Yao, S. Yang, *Adv. Funct. Mater.* **2021**, *31*, 2102350; d) X. Li, C. Cao, C. Liu, W. He, K. Wu, Y. Wang, B. Xu, Z. Tian, E. Song, J. Cui, G. Huang, C. Zheng, Z. Di, X. Cao, Y. Mei, *Nat. Commun.* **2022**, *13*, 7819; e) Y. Liu, S. Song, H. Yoon, M. Liu, L. Yang, D. Ge, *Sol. Energy Mater. Sol. Cells* **2022**, *238*, 111611; f) J. Son, J. A. Kim, B. S. Joo, W. Y. Lee, J. Kang, I. K. Han, H. S. Jang, H. Ko, G. Kang, *Solar RRL* **2023**, *7*, 2300445; g) W. Wang, H. Lai, Z. Cheng, Z. Fan, D. Zhang, J. Wang, S. Yu, Z. Xie, Y. Liu, *ACS Appl. Mater. Interfaces* **2020**, *12*, 49219; h) X. Yang, S. Lv, T. Li, S. Hao, H. Zhu, Y. Cheng, S. Li, H. Song, *ACS Appl. Mater. Interfaces* **2022**, *14*, 20083.
[9] a) Y. Li, J. Lin, H. Guo, W. Sun, S. Xiao, L. Zhou, *Adv. Opt. Mater.* **2020**, *8*, 1901548; b) H. Palamadathil Kannattil, L. Martinez Soria Gallo, K. D. Harris, B. Limoges, V. Balland, *Adv. Sci.* **2024**, *11*, 2402369; c) J. Pu, M. Han, C. Shen, J. Wang, L. Lu, *Adv. Sci.* **2024**, *11*, 2401991; d) C. Su, Z. Zhao, D. He, H. Song, C. Zhao, W. Mai, *Nano Energy* **2023**, *111*, 108396; e) C. Zhang, J. Yang, Y. Li, J. Song, J. Guo, Y. Fang, X. Yang, Q. Yang, D. Wang, X. Deng, *Adv. Funct. Mater.* **2022**, *32*, 2208144.
[10] S. Tan, S. Guo, Y. Wu, T. Zhang, J. Tang, G. Ji, *Adv. Funct. Mater.* **2024**, *35*, 2415921.
[11] a) M. Nakano, K. Shibuya, N. Ogawa, T. Hatano, M. Kawasaki, Y. Iwasa, Y. Tokura, *Appl. Phys. Lett.* **2013**, *103*, 153503; b) J. Sang, W. Zhu, Y. Feng, Y. Liu, J. Shang, J. Sun, L. Guo, Y. Zhang, S. Zhao, V. Chigrinov, D.-S. Seo, *ACS Appl. Electron. Mater.* **2021**, *3*, 4882; c) Y. Cui, Y. Ke, C. Liu, Z. Chen, N. Wang, L. Zhang, Y. Zhou, S. Wang, Y. Gao, Y. Long, *Joule* **2018**, *2*, 1707.
[12] a) C. Jiang, L. He, Q. Xuan, Y. Liao, J.-G. Dai, D. Lei, *Light: Sci, Appl.* **2024**, *13*, 255; b) H. Sun, L. Lin, L. Zhang, H. Liu, C. Dong, C. Li, W. Mi, D. Wang, L. He, L. Zhou, *J. Mater. Sci.:Mater. Electron.* **2024**, *35*, 2086.
[13] Z. Chen, Y. Gao, L. Kang, C. Cao, S. Chen, H. Luo, *J. Mater. Chem. A* **2014**, *2*, 2718.
[14] Y. Zhou, S. Wang, J. Peng, Y. Tan, C. Li, F. Y. C. Boey, Y. Long, *Joule* **2020**, *4*, 2458.
[15] Q. Chang, Z. Shen, Z. Guo, C. Xue, N. Li, J. Yang, S. Hu, *ACS Appl. Mater. Interfaces* **2021**, *13*, 12375.
[16] B. Li, F. Xu, T. Guan, Y. Li, J. Sun, *Adv. Mater.* **2023**, *35*, 2211456.
[17] R. L. Sala, R. H. Gonçalves, E. R. Camargo, E. R. Leite, *Sol. Energy Mater. Sol. Cells* **2018**, *186*, 266.
[18] Y. Ding, Y. Duan, F. Yang, Y. Xiong, S. Guo, *Chem. Eng. J.* **2023**, *460*, 141572.
[19] G. Chen, K. Wang, J. Yang, J. Huang, Z. Chen, J. Zheng, J. Wang, H. Yang, S. Li, Y. Miao, W. Wang, N. Zhu, X. Jiang, Y. Chen, J. Fu, *Adv. Mater.* **2023**, *35*, 2211716.
[20] K. Wang, G. Chen, S. Weng, L. Hou, D. Ye, X. Jiang, *ACS Appl. Mater. Interfaces* **2023**, *15*, 4385.
[21] F. Chen, G. Lu, H. Yuan, R. Li, J. Nie, Y. Zhao, X. Shu, X. Zhu, *J. Mater. Chem. A* **2022**, *10*, 18235.
[22] G. Chen, K. Wang, J. Yang, J. Huang, Z. Chen, J. Zheng, J. Wang, H. Yang, S. Li, Y. Miao, W. Wang, N. Zhu, X. Jiang, Y. Chen, J. Fu, *Adv. Mater.* **2023**, *35*, 2211716.
[23] K. Midtdal, B. P. Jelle, *Sol. Energy Mater. Sol. Cells* **2013**, *109*, 126.
[24] B. S. Yilbas, H. Ali, M. M. Khaled, N. Al-Aqeeli, N. Abu-Dheir, K. K. Varanasi, *Sci. Rep.* **2015**, *5*, 15833.
[25] X. Yao, Y. Hu, A. Grinthal, T.-S. Wong, L. Mahadevan, J. Aizenberg, *Nat. Mater.* **2013**, *12*, 529.
[26] K. Manabe, T. Matsubayashi, M. Tenjimbayashi, T. Moriya, Y. Tsuge, K.-H. Kyung, S. Shiratori, *ACS Nano* **2016**, *10*, 9387.
[27] J. Chen, S. Cao, Y. Liu, S. Qin, H. Li, T. Yang, J. Zhao, B. Zou, *Adv. Energy Mater.* **2024**, *15*, 2403414.
[28] K. Yin, J. Wu, Q. Deng, Z. Wu, T. Wu, Z. Luo, J. Jiang, J.-A. Duan, *Chem. Eng. J.* **2022**, *434*, 134756.
[29] S. G. Lee, D. Y. Lee, H. S. Lim, D. H. Lee, S. Lee, K. Cho, *Adv. Mater.* **2010**, *22*, 5013.
[30] X. Yao, J. Ju, S. Yang, J. Wang, L. Jiang, *Adv. Mater.* **2013**, *26*, 1895.
[31] C. Chen, Z. Huang, S. Zhu, B. Liu, J. Li, Y. Hu, D. Wu, J. Chu, *Adv. Sci.* **2021**, *8*, 2100701.
[32] Y. Li, Y. Zhang, J. Zhang, X. Li, J. Liu, Z. Guo, X. Liu, H. Zheng, *ACS Appl. Mater. Interfaces* **2025**, *17*, 42205.
[33] W. Xu, H. Zheng, Y. Liu, X. Zhou, C. Zhang, Y. Song, X. Deng, M. Leung, Z. Yang, R. X. Xu, Z. L. Wang, X. C. Zeng, Z. Wang, *Nature* **2020**, *578*, 392.
[34] Y. Jin, S. Yang, M. Sun, S. Gao, Y. Cheng, C. Wu, Z. Xu, Y. Guo, W. Xu, X. Gao, S. Wang, B. Huang, Z. Wang, *Nat. Commun.* **2024**, *15*, 4762.
[35] Y. Li, X. Qin, Y. Feng, Y. Song, Z. Yi, H. Zheng, P. Zhou, C. Wu, S. Yang, L. Wang, P. Zhu, W. Xu, Z. Wang, *Droplet* **2024**, *3*, 91.
[36] a) C. Chen, S. Guo, L. Zhang, H. Yao, B. Liu, C. Zhang, Y. Zhang, Z. Lao, S. Wu, D. Wu, *Int. J. Extreme Manuf.* **2024**, *7*, 015504; b) C. Chen, H. Yao, S. Guo, Z. Lao, Y. Xu, S. Li, S. Wu, *Adv. Funct. Mater.* **2022**, *33*, 2210495; c) Y. Hu, C. Chen, C. Wang, Q.-F. Guan, Y. Hu, J. Ni, D. Wu, S.-H. Yu, *Nano Lett.* **2025**, *25*, 1520; d) Z. Lao, X. Liu, Q. Qi, H. Hu, M. Liu, H. Zhu, R. Dong, Y. Zhang, S. Wu, C. Zhang, C. Chen, L. Zhang, *Adv. Funct. Mater.* **2025**, *35*, 2423425; e) X. Yang, L. Liang, C. Li, B. Zhang, Y. Zhao, S. Tan, G. Ji, *Nano Lett.* **2024**, *25*, 569; f) K. Yin, L. Wang, Q. Deng, Q. Huang, J. Jiang, G. Li, J. He, *Nano-Micro Lett.* **2022**, *14*, 97; g) S.-Y. Yin, Q. Guo, S.-R. Liu, J.-W. He, Y.-S. Yu, Z.-N. Tian, Q.-D. Chen, *Opto-Electron. Sci.* **2024**, *3*, 240003; h) Y. Yuan, L. Jiang, X. Li, P. Zuo, X. Zhang, Y. Lian, Y. Ma, M. Liang, Y.

Zhao, L. Qu, *Adv. Mater.* **2022**, *34*, 2110013; i) C. Zhang, Q. Yang, H. Li, Z. Luo, Y. Lu, J. Zhang, C. Li, F. Chen, *Int. J. Extreme Manuf.* **2025**, *7*, 035004.
[37] a) G. Cui, P. Zhang, X. Liu, L. Xie, W. Huang, P. Pan, J. Qu, Q. Fan, *IEEE Trans. Ind. Electron.* **2023**, *70*, 10302; b) X. Li, C. Lu, Z. Song, W. Ding, X.-P. Zhang, *IEEE Rob. Autom. Lett.* **2022**, *7*, 9264.
[38] D. Son, M. C. Ugurlu, M. Sitti, *Sci. Adv.* **2021**, *7*, abi8932.
[39] Y. Zhao, S. Tan, J. Yu, R. Yu, T. Xu, J. Zheng, G. Ji, *Adv. Mater.* **2024**, *37*, 2412845.
[40] X.-H. Li, C. Liu, S.-P. Feng, N. X. Fang, *Joule* **2019**, *3*, 290.
[41] Z. Na, X. Liang, H. Wang, L. Yu, C. Fan, Q. Wang, X. Wang, H. Yang, *Adv. Funct. Mater.* **2023**, *34*, 2308312.
[42] S. Perumanath, R. Pillai, M. K. Borg, *Nano Lett.* **2023**, *23*, 4234.
[43] N. Zhang, H. Zhang, Z. Liu, W. Xu, H. Zheng, Y. Song, Z. Wang, X. Zhou, *Nano Energy* **2023**, *106*, 108111.
[44] K. Wang, W. Xu, J. Li, H. Zheng, S. Sun, W. Song, Y. Song, Z. Ding, R. Zhang, Y. Sun, H. Zhang, J. Li, Z. Wang, *Nano Energy* **2023**, *111*, 108388.
[45] M. Liao, W. Xu, Y. Song, Z. Pan, H. Zheng, Y. Li, X. Qin, L. Wang, J. Lu, Z. Wang, *Nano Energy* **2023**, *116*, 108831.